Measurement Science
and Technology

100 year anniversary
Measurement Science and Technology

PURPOSE-LED
PUBLISHING™

PAPER • OPEN ACCESS

Event-based particle image velocimetry for high-speed flows

To cite this article: Christian Willert 2025 *Meas. Sci. Technol.* **36** 075302

OPEN ACCESS
IOP Publishing
Measurement Science and Technology
Meas. Sci. Technol. **36** (2025) 075302 (12pp)
https://doi.org/10.1088/1361-6501/ade27a

Event-based particle image velocimetry for high-speed flows

Christian Willert

DLR Institute of Propulsion Technology, Deutsches Zentrum für Luft- und Raumfahrt (DLR), 51170 Köln, Germany

E-mail: chris.willert@dlr.de

Received 27 March 2025, revised 28 May 2025
Accepted for publication 9 June 2025
Published 24 June 2025

Abstract

The article describes the implementation of a particle image velocimetry system based on event-based vision (EBV) capable of providing time-resolved, two-component flow field data at frame rates exceeding 2.5 kHz. Compared to previous event-based imaging velocimetry (EBIV)systems the present setup is applicable to high-speed flows in the transonic regime and beyond. At the core of the measurement principle is the separation of the two laser pulses onto two imaging channels. Using orthogonally polarized pulses of light to illuminate micrometer sized particles carried with the flow, the dual-EBV camera setup incorporates a polarizing beam-splitter cube to redirect the scattered polarized light onto the respective EBV detectors. The proposed high-speed EBIV measurement approach is demonstrated on a high-speed ($\mathrm{Ma} = 0.5$) free jet with inter-pulse delays down to 100 ns. For cases in which polarization separation cannot be realized, a two-color illumination of the particles with a dichroic mirror on the camera side is proposed.

Keywords: event-based imaging, high-speed imaging, particle image velocimetry, PIV, neuromorphic imaging

1. Introduction

The recently introduced event-based imaging velocimetry (EBIV) [1] and its variant using pulsed illumination [2] have demonstrated the potentials of the novel event-based vision (EBV) technology in particle-based flow diagnostics. The underlying imaging approach of EBV marks a departure from the ubiquitous frame based imaging concepts by reporting only intensity changes within the imaged scene whereas the original intensity level is not recorded. Each pixel of the EBV sensor acts individually detecting and reporting changes of intensity exceeding a certain threshold, typically 5%–20%. Since the detection is sourced in the relative measurement of intensity, rather than an absolute intensity measurement of conventional cameras, a very high dynamic range can be achieved, typically exceeding >120 db or 20 bit equivalent. The data streamed from an EBV sensor—quadruplets of position coordinates, time-stamp and polarity of the contrast change—is asynchronous by nature and scales linearly with the amount of temporal contrast change in the observed scene.

EBV's initial concepts were originally conceived in the 1990s [3, 4], followed by a continuous development that ultimately resulted in the present-day, ready-to-use and affordable EBV cameras [5]. Acting as a technology enabler, EBV has already found applications in a wide variety of fields [6] with flow diagnostics comprising one sub-field, mostly for 3d particle tracking velocimetry of sparsely seeded flows [7–10] as well as planar (2d 2c) velocimetry [1, 2, 11–13].

This present work proposes an approach for extending EBIV to applications in high-speed flows by addressing the issues of technology-specific limitations concerning the sensor's response time through a combination of two EBV cameras. As with any detection device, the pixel and adjoining

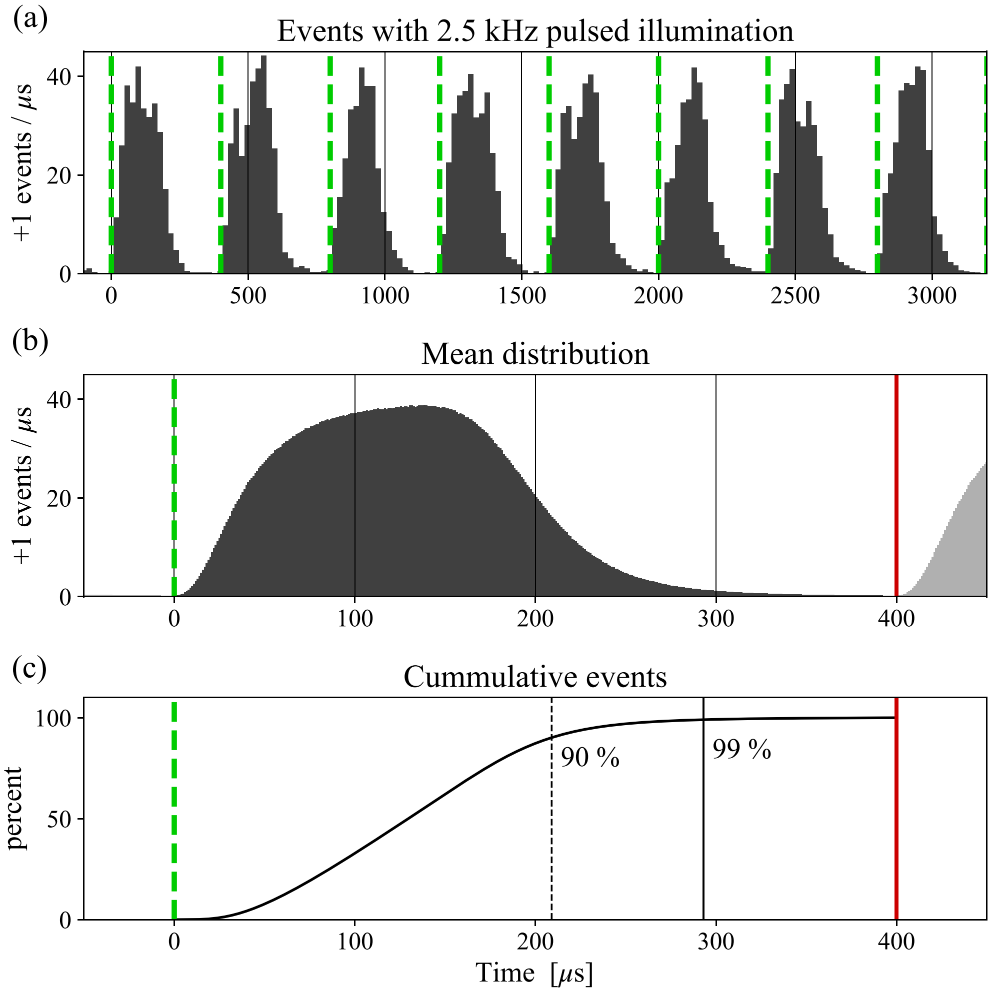

Figure 1. Histograms of positive events recorded by an EBV camera in response to pulsed illumination of small particles at 2.5 kHz (positive event rate 16.3×10^6 s); events during 8 laser pulse intervals with green vertical lines indicating the laser pulses (a), mean event histogram compiled over 2 s (b), red line indicates end of period, cumulative event distribution (c).

read-out circuitry of the EBV sensor has a finite response time (latency) that varies between different sensor architectures and depends on lighting conditions among a number of other parameters. The hardware used in the present study has a quoted response latency of 100 µs at an illuminance of 1 klx [14, 15] which facilitates imaging at an equivalent frame rate of 10 kHz. The latency increases with the event rate reaching a maximum of 200 µs to 300 µs once the sensor's readout registers (arbiters) begin to saturate. At the same time the latency introduces an uncertainty between the actual contrast change occurrence and the time-stamp assigned to the registered event. In event-based imaging velocimetry (EBIV) this uncertainty was overcome by illuminating the particle field with a pulsed light source, either by a short-pulse laser or pulse-modulated continuous light source (LED, CW-laser) [2].

An example of the EBV camera's registered event stream in response to the pulsed illumination is given in figure 1. Due to the camera's latency it requires nearly 300 µs to transfer 99 % of the events induced for a given light pulse. For this specific event rate, the light pulsing could be increased to about 3.3 kHz without cross-talk of a given set of events into the following laser pulse period. Consequently, the minimum time interval for particle imaging, that is the temporal separation of two adjacent light pulses, Δt, is restricted to values greater than 300 µs. In [2] is was demonstrated that pseudo-framing rates exceeding 5 kHz are feasible. By reducing the active imaging area the rate can be raised beyond 10 kHz.

In the context of particle image velocimetry (PIV) the minimal light-pulse separation $\Delta t_{\min}$ is equivalent to the previously introduced latency which limits the application to flows of moderate velocity (e.g. ≈2–5 m s^{-1} on a 100 mm field of view (FOV)). To reduce Δt to below the camera's framing period, modern frame-based cameras employ the so-called 'frame-straddling' technique by placing a light pulse toward the end of one frame followed by a second pulse at the beginning of the following frame [16]. With the EBV sensor continuously active, the frame-straddling approach cannot be employed for EBIV to capture flows requiring a pulse delay Δt below the aforementioned latency. To nonetheless allow the capture of high-speed flows with EBV this contribution follows the approach of separating the light scattered by the particles into two channels that ideally have no cross-talk. In the present configuration this channel separation is realized by illumination of the particle field with two different polarizations of the incident light. For particles in the micrometer size range the polarization is preserved for the scattered light (Mie scattering regime). Channel separation may also be achieved using two different wavelengths for particle illumination; a dichroic mirror in the optical path then directs the scattered light to the respective cameras.

Polarization separation has been in use in the field of PIV since its beginning. For single-frame double-exposure, photography-based PIV a birefringent crystal plate placed in the imaging path was used to offset the second light pulse sufficiently to extend the measurement range to zero and beyond (direction ambiguity removal [17]). For stereoscopic dual-plane PIV, polarization separation was used to simultaneously capture two parallel light sheet planes onto two camera pairs [18]. In a similar way, the multi-pulse shake-the-box (STB) method extends the STB approach to high-speed flows by using differently polarized light and polarizing beam-splitters (P-BSs) to record 4 image frames in short succession [19, 20].

Imaging approaches that discretely capture single pulses of scattered light onto separate imaging sensors, either by beam-splitter or rotating mirror, is also very common in the field of high-speed imaging [21]. A beam-splitter cube in the optical path allows the simultaneous view of the same FOV enabling image pair capture within a short time interval, depending on the shutter speed of the sensors [22]. A combination of three beam-splitter cubes allowed the capture of four separate images [23] or eight images using dual-framing cameras [24].

The following article first introduces a dual EBV camera prototype using a P-BS for channel separation, demonstrating it with measurements on a high-speed free jet. Further validation measurements are performed with a compact single-lens, dual camera-system, which is then used to capture the time-resolved cylinder wake in a small windtunnel. Converged flow statistics and results from spectral modal decomposition (SPOD) demonstrate the feasibility of the proposed measurement approach.

2. Implementation and validation

2.1. Dual EBV camera setup

Figure 2 provides a schematic of the implemented high-speed EBIV system using a pair of EBV cameras (Prophesee, EVK4 and Century Arks, SilkyEvCam-HD). The cameras are based on the Sony IMX636 EBV sensor which feature 4.86 µm pixels in an array of 1280 × 720 size [15]. Each camera is fitted with a macro-lens (Nikon Micro-Nikkor 55 mm f/2.8) and observe a common FOV through a P-BS cube (Thorlabs PBS251, 25.4 mm, 420–680 nm). External synchronization is provided by an 1 MHz clock such that there is no timing drift between the cameras. In addition a 10 Hz pulse is continuously recorded by the cameras to allow *a posteriori* alignment of the individually recorded event streams. This is necessary as each camera operates in its own processing thread with recording triggered through system messaging within the host operating system (on MS-Windows v.10/11 the offset between the software triggered recordings is in range of 20 ms to 100 ms). A photograph of the imaging configuration on a free jet is shown in figure 3.

On the illumination side the beams from a pair of high-speed lasers (Innolas/Iradion NanioAir 532) are combined into a common beam using a P-BS cube. As both lasers are vertically polarized at their beam exit, the polarization of one system (Laser 2 in figure 2) is rotated by 90° using a half-wave plate ($\lambda/2$). This is necessary for the beam combination by the P-BS. Normally the combined light is then circularly polarized using a quarter-wave plate ($\lambda/4$), however, in the present application this component is removed in order to implement the proposed dual EBV camera particle imaging approach.

2.2. Event record acquisition and processing

Optimal performance of the dual event-camera configuration is achieved when the event-data rates are balanced between the cameras. This can be monitored during acquisition and is fine-tuned by adjusting the pulse energy of the respective lasers. The lasers' pulse energy and overall seeding particle density determine the effective event rate and are adjusted while monitoring the temporal distribution of the events (see figure 4) making sure that there is no cross-talk of events into the following laser pulse period. The cameras' biases are set to identical values and should favor the generation of positive events since the negative events were found unsuitable in the context of pulsed particle illumination [2].

The processing of the acquired event streams can be split into two main parts as illustrated in figure 5. The first step involves the temporal alignment of the records using the 10 Hz reference markers within the records. Currently this is done manually but could be automated using a high cross-correlation signal between pseudo-frames of both cameras as a match-indicator. The aligned records are then converted into matching pairs of pseudo-frames with the framing rate matching the laser pulsing rate and stored in a compressed multi-page image file format. In the second step, cross-correlation based PIV processing recovers the (uncorrected) displacement fields for each pseudo-image pair.

To obtain the actual displacement field the displacement due to the misalignment between the two cameras has to be subtracted. This *disparity map* is obtained by recording the flow field with both lasers pulsing at the same time (i.e. $\Delta t = 0$) over a number of pulsing periods ($N = 100$–1000). The processing follows the previously described steps and yields a mean displacement field. Shift, rotation and magnification difference between the camera's EBV sensors can be well described using second order polynomials obtained through standard least-squares fitting such as shown in figure 6(a). In this realization the maximum sensor misalignment is less than 10 pixel (≈50 µm) with a center of rotation near the top edge.

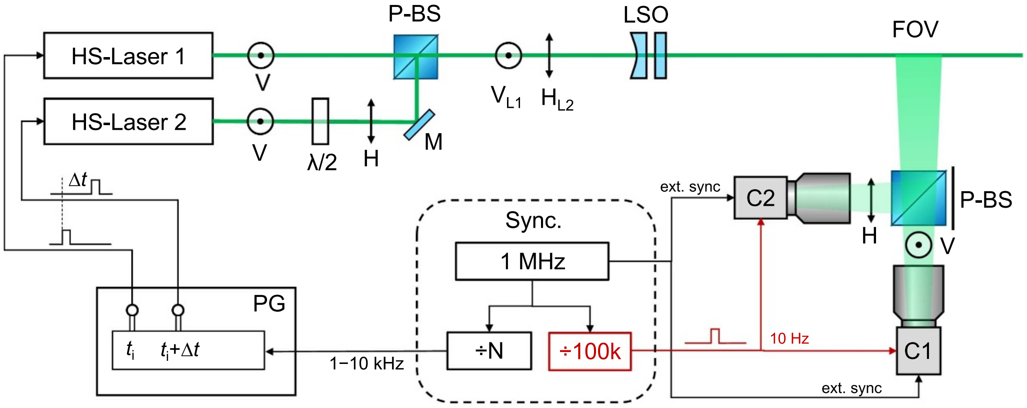

Figure 2. Dual-EBV camera setup for high-speed PIV. Light polarization is either horizontal (↕) or vertical (⊙), polarizing beam-splitter cube (P-BS), half-wave plate ($\lambda/2$), mirror (M), light sheet forming optics (LSO), pulse generator (PG).

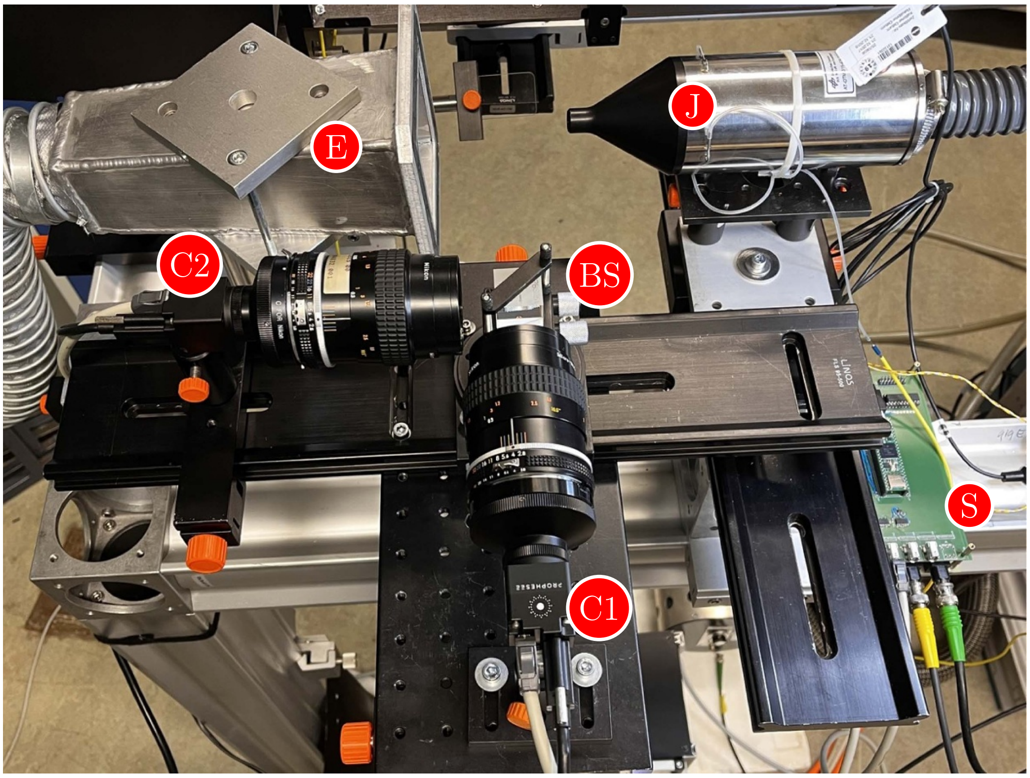

Figure 3. Prototype dual-EBV camera setup for measurements on high-speed free jet. (C1), (C2) event cameras, (J) free jet, (E) exhaust, (S) synchronizer circuit. Dual laser system and light sheet optics are located below the camera system (not visible).

The residuals (cf figure 6(b)) have a mean (rms) deviation on the order 1/100 of a pixel and exhibit a spatially periodic structure that could be ascribed to pixel-locking artifacts. The binary and often single-pixel sized event-based particle imagery is more susceptible to pixel-locking than conventional gray-scale PIV recordings. While low-pass filtering can be used to attenuate the pixel-locking, it cannot remove it.

2.3. *Validation measurements on a free jet*

The dual EBV camera imaging approach is validated with measurements within the constant velocity core region of a high-speed free jet with exit velocities up to $180\,\mathrm{m\,s^{-1}}$ ($\mathrm{Ma} = 0.53$). The jet flow is seeded with $\approx 1\,\mu\mathrm{m}$ paraffin droplets atomized by a Laskin type seeding generator and injected into the intake of the radial air compressor that supplies the jet. For these measurements the external flow was not seeded such that the jet's shear layers are only partially seeded. Seeding concentration and laser power was adjusted to achieve on the order of $10–50 \times 10^6\,\mathrm{Events\,s^{-1}}$.

Measurements are acquired at $f_{\mathrm{Laser}} = 1\,\mathrm{kHz}$ and $2.5\,\mathrm{kHz}$ at event rates close to the maximum feasible without camera saturation (event-overflow) which is of $O(30–40 \times 10^6\,\mathrm{Events\,s^{-1}})$ for the used camera models (Prophesee

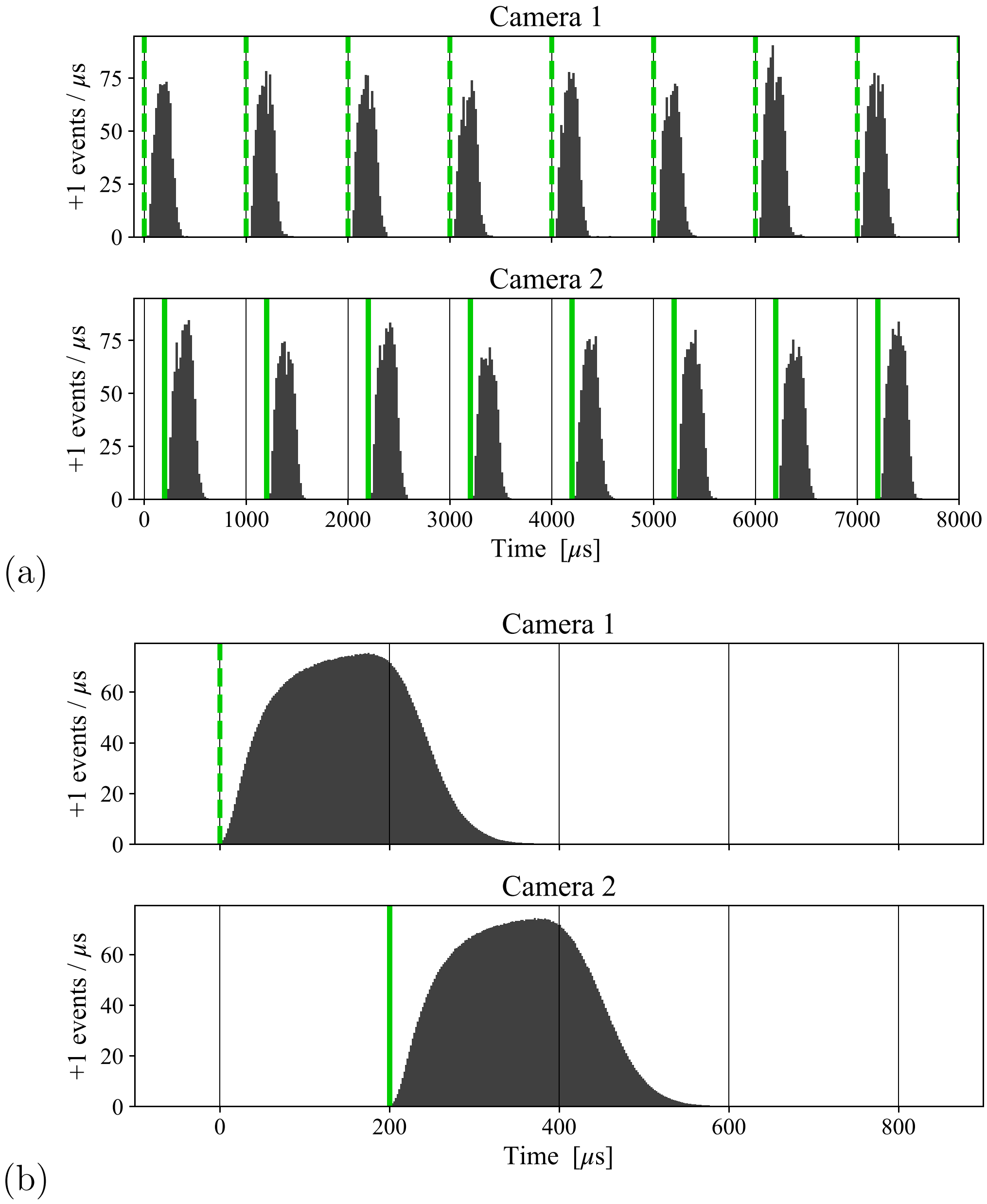

Figure 4. Histograms of event data streams simultaneously recorded by a pair of EBV cameras in response to orthogonal polarized laser pulse pairs at 1 kHz; (a) events during 8 laser pulse intervals with green vertical lines indicating the laser pulses, (b) mean event histograms ($\Delta t = 200\,\mu$s laser pulse pair separation, positive event rate camera1 / camera-2: 15.8×10^6 / 15.6×10^6 Events s^{-1}).

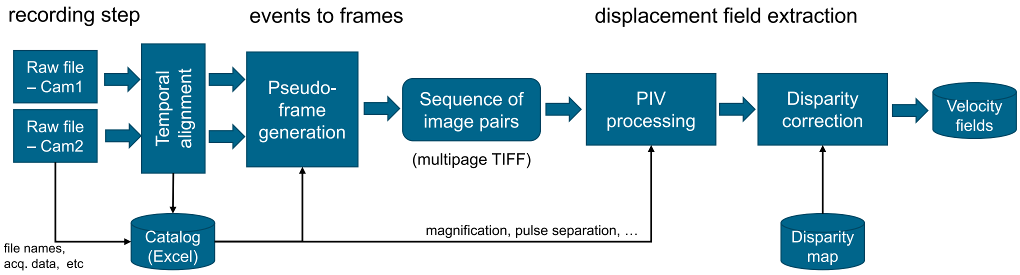

Figure 5. Off-line processing scheme for retrieval of flow field data from event recordings captured by the two EBV cameras.

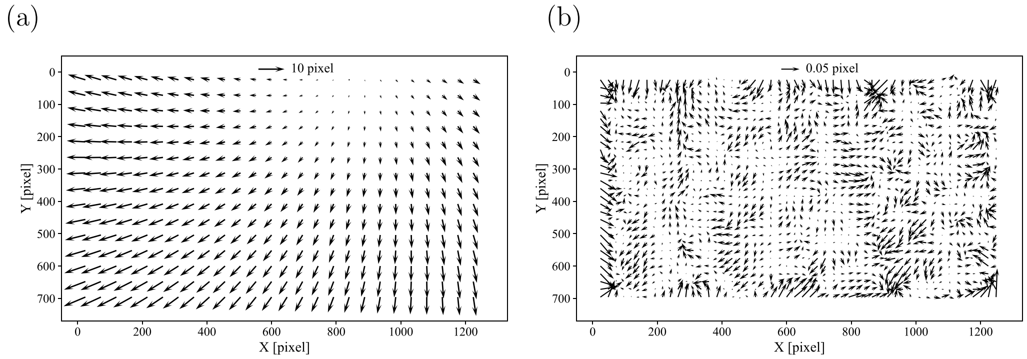

Figure 6. (a) Second order least-square fit to mean camera offset obtained from a free jet flow with $\Delta t = 0$; (b) residuals of least-squares fit ($\sigma_x = 0.0138$ pixel, $\sigma_y = 0.0147$ pixel).

EVK-4, Century Arks SilkyEvCam-HD). Since the event processing only involves positive events, the usable event rate is limited to roughly half this value ($15 \times 10^6 - 20 \times 10^6$ +Events s^{-1}). For presently used pulsed illumination the negative events are only weakly correlated with the light pulses but are nonetheless captured in the recording process.

With the imposed hardware limitation on event transfer, the number of events on a given pseudo-frame is limited. At a laser pulsing frequency of $f_{\text{Laser}} = 2.5$ kHz about 5000–6000 positive events are recorded per pseudo-frame increasing to O(12 000–16 000) at 1 kHz. The average particle image size is of O(1.3–1.5 pixel) and strongly depends on lens focus such that about 10 000 particles can be imaged at 1 kHz (or about 4000 particles/frame at 2.5 kHz). The corresponding particle image density at 1 kHz is on the order of 0.010–0.012 particles per pixel (ppp), decreasing to O(0.004–0.006 ppp) at 2.5 kHz. For a sampling window of size 48 × 48 pixels this translates to about 25 particles per sample at 1 kHz or about 11 particles per sample at 2.5 kHz.

Using macroscopic imaging the FOV captured by the camera system covers 17.2 mm × 9.7 mm (magnification 13.5 µm/pixel, $m = 0.362$) with both lenses set to an aperture of f/4. The light sheet has a thickness of about 500 µm and is spread to roughly 30 mm width at the FOV. A calibrated thermopile (Model BB25, SLT Sensor & Lasertechnik GmbH) measured an energy of 40 µJ to 50 µJ per pulse.

Recordings of 5 s duration are obtained at the different laser pulse separations from $\Delta t = 100$ ns to 3 µs. In addition, recordings of 2 s duration at $\Delta t = 0$ are used to quantify the sensor misalignment (e.g. disparity map). This can be performed as part of the actual experiment, that is, while the jet is operating.

After stabilization of the jet flow, verified through constant plenum pressure and temperature, measurements are acquired at two conditions. With a nozzle diameter of 10 mm the jet's Reynolds number corresponds to $\text{Re}_D = U_{\text{jet}} D_{\text{jet}} / \nu = 84\,500$ at $U_{\text{jet}} = 124.9\,\text{m s}^{-1}$ (Ma = 0.36) and $\text{Re}_D = 128\,000$ at $U_{\text{jet}} = 182.6\,\text{m s}^{-1}$ (Ma = 0.53). Figure 7 presents the mean velocity field for $\Delta t = 1.0$ µs for the high-Re condition immediately downstream of the nozzle which is located at $x = 0$. Velocity statistics are sampled at the centerline as shown in figure 7 and are provided in figure 8. For both conditions the mean varies by less than 0.2% for $\Delta t \geqslant 0.3$ µs. The error bars indicate the root mean square (RMS) values of the axial velocity which decrease with increasing pulse delay. Table 1 provides the data for the high Re_D condition in pixel units and

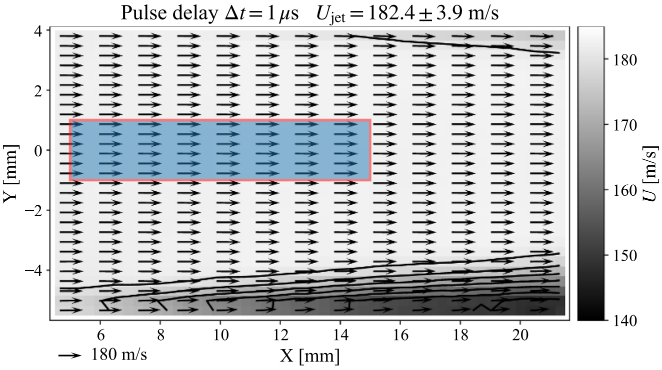

Figure 7. Mean free jet core flow at $U_\infty = 180\,\text{m s}^{-1}$ recorded with a pulse delay of 1 µs downstream of the nozzle at $0.46 \leqslant x/D \leqslant 2.13$. Shaded area indicates sampling domain for velocity statistics.

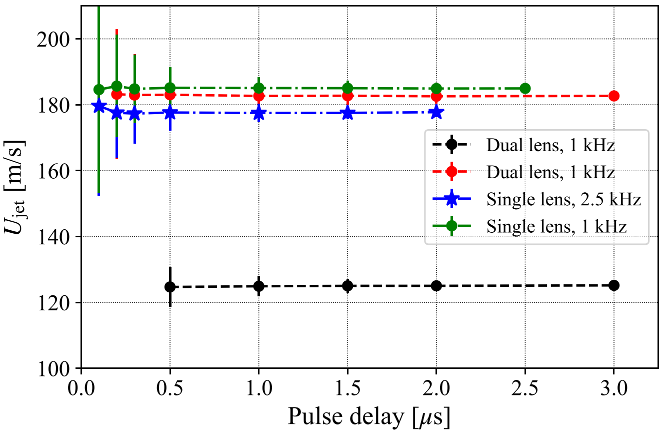

Figure 8. Mean flow statistics obtained along the centerline at $x/D = 1$ obtained for different pulse delays Δt at pulsing frequencies of $f_{\text{Laser}} = 1$ kHz (red, black, green lines) and 2.5 kHz (blue line). The single-lens configuration is introduced in section 2.4.

Table 1. Mean and RMS of both displacement components within the jet core flow. 'Filtered' values obtained by subtracting global camera vibration of 75 Hz, interrogation with 48 × 48 pixel.

Δt (μs)	f_{Laser} (Hz)	Δx (px)	Δx_{rms} (px)	$\Delta x_{\text{rms,filt}}$ (px)	Δy (px)	Δy_{rms} (px)	$\Delta y_{\text{rms,filt}}$ (px)
0	2500	0.014	0.220	0.040	0.0070	0.210	0.039
0.2	2500	2.691	0.211	0.044	−0.0058	0.196	0.041
0.3	2500	4.040	0.218	0.046	−0.0107	0.205	0.042
0.5	2500	6.747	0.211	0.051	−0.0135	0.208	0.047
1.0	2500	13.44	0.216	0.065	−0.0329	0.190	0.060
1.5	2500	20.21	0.200	0.080	−0.0629	0.168	0.077
2.0	2500	26.90	0.207	0.095	−0.0837	0.193	0.094
3.0	2500	40.38	0.233	0.131	−0.1229	0.214	0.131

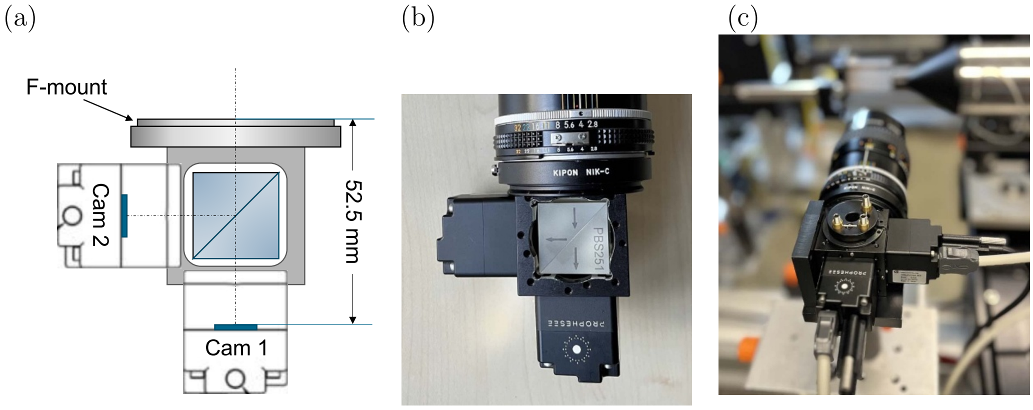

Figure 9. Dual EBV sensor configuration using a single imaging lens, schematic (a), camera assembly showing beamsplitter (b), setup for free jet measurements (c).

indicate that the RMS pixel displacements are nearly constant at about 0.2 pixel across the range of pulse delays.

Inspection of the data revealed a periodic offset of the sensors with respect to each other at a constant frequency of 75 Hz that is modulated onto both components of the displacement field. This is caused by the cantilevered mounting of the cameras in the prototype setup. Subtraction of this dynamic component results in estimates of the RMS fluctuations of displacement that start from 0.04 pixel at zero displacement increasing to 0.131 pixel at a shift of 40 pixels.

2.4. *Single lens camera setup*

To both ease the lens focusing process and to alleviate vibration issues with the cantilevered camera mounting, a second variant of the dual EBV camera setup was realized. As illustrated in figure 9 both cameras are rigidly fixed to two sides of a 40 mm mounting cube (Qioptiq, Cube 30, G061081000). A lens mounting ring (Nikon F-mount) on a third cube face supports interchangeable 35 mm format objective lenses. Due to the presence of the glass cube with an index of refraction $N = 1.725$ the flange distance is increased from the nominal 46.5 mm to 64.6 mm (cf figure 9(a)). To facilitate alignment of the sensor pair to within a few pixels the beam-splitter cube is mounted inside the cube on a adjustable 3-axis prism support (Qioptiq, G063731000). Residual misalignment is accounted for by the previously described methodology using 'flow field data' acquired at $\Delta t = 0\,\mu\text{s}$.

Measurements of the free jet are repeated with a magnification of 9.11 μm/pixel ($m = 0.53$) for the high-Re condition at $f_{\text{Laser}} = 1\,\text{kHz}$ and 2.5 kHz. The mean velocity is plotted as a blue dash–dotted line in figure 7 and corresponding displacement statistics are provided in table 2. The axial flow component u exhibits distinct frequency peaks (see figure 10) that are sourced in the radial compressor driving the jet. To obtain estimates of the measurement uncertainty, the raw data is filtered by subtracting the mean displacement from each velocity record before computing the statistics. The documented measurement uncertainties $\Delta x_{\text{rms}} = 0.03$–$0.06$ pixel are of similar magnitude as for conventional 2-frame PIV.

3. Application to cylinder wake flow

The wake flow of a cylinder in a small windtunnel is chosen as a proxy for a complex flow to demonstrate the performance of the dual event-camera EBIV implementation. In the setup a cylinder of diameter $D = 9.5\,\text{mm}$ spans the midsection of a square channel of $L = 76\,\text{mm}$ side length and corresponding blockage ratio $D/L = 12.5\%$. The bulk flow in the channel was set to approximately $U_b = 6.7\,\text{m}\,\text{s}^{-1}$, as measured with conventional high-speed PIV (HSPIV). This corresponds to a cylinder Reynolds number of $\text{Re}_D = 4200$ and $\text{Re}_L = 34\,000$

Table 2. Mean and RMS of both displacement components within the jet core flow obtained with the single lens—dual-camera setup. ‘Filtered’ values are obtained by subtracting global mean, interrogation with 32 × 32 pixel at laser pulsing frequency of 1 kHz and 48 × 48 pixel at 2.5 kHz.

Δt (µs)	f_{Laser} (Hz)	Δx (px)	Δx_{rms} (px)	$\Delta x_{\mathrm{rms,filt}}$ (px)	Δy (px)	Δy_{rms} (px)	$\Delta y_{\mathrm{rms,filt}}$ (px)
0.0	1000	0.023	0.133	0.025	0.0093	0.028	0.025
0.1	1000	2.022	0.137	0.026	0.025	0.029	0.026
0.2	1000	4.066	0.138	0.026	0.047	0.029	0.027
0.3	1000	6.071	0.136	0.027	0.070	0.032	0.028
0.5	1000	10.14	0.139	0.027	0.117	0.034	0.032
1.0	1000	20.26	0.145	0.031	0.234	0.046	0.044
1.5	1000	30.39	0.155	0.035	0.346	0.061	0.060
2.0	1000	40.50	0.170	0.038	0.462	0.078	0.078
2.5	1000	50.63	0.187	0.043	0.575	0.094	0.095
0.0	2500	0.0005	0.145	0.031	0.0012	0.035	0.031
0.1	2500	1.970	0.144	0.031	0.020	0.036	0.032
0.2	2500	3.896	0.146	0.032	0.040	0.037	0.033
0.3	2500	5.835	0.147	0.032	0.060	0.038	0.035
0.5	2500	9.744	0.149	0.034	0.103	0.041	0.039
1.0	2500	19.47	0.157	0.041	0.211	0.053	0.053
1.5	2500	29.21	0.167	0.050	0.316	0.069	0.071
2.0	2500	39.00	0.184	0.061	0.422	0.084	0.088

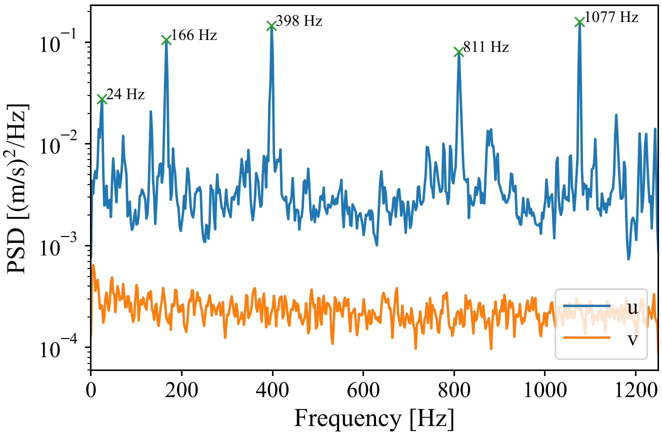

Figure 10. Frequency spectrum for both velocity components of the jet core flow obtained with the single lens—dual-camera setup.

for the square channel. At a magnification of 30.8 µm/pixel the FOV covers an area of 39.5 × 22.2 mm^2 and is located immediately downstream of the cylinder to capture the formation of the vortex shedding.

Akin to the measurements of the free jet, the inter-camera offset is determined from recordings obtained with a pulse delay of $\Delta t \approx 0$ (a pulse-to-pulse jitter of ±5 ns was observed). At $\Delta t = 25$ µs the free stream produces a particle displacement of about 10 pixels for the chosen image magnification. With the laser pulsing rate fixed at $f_{\mathrm{Laser}} = 1.25$ kHz, seeding density, laser power and camera biases were adjusted to achieve a positive (+1) event rates of up to 50 × 10^6 Events s^{-1} per camera. This resulted in a particle image density of about 0.025 ppp (particles per pixel) or about 25 000 particle images per pseudo-frame. Multiple records of 5 s duration were acquired and converted to pseudo-frame sequences that were then PIV processed with sample sizes of 48 × 48 pixel. Additional measurements were obtained at a reduced sensor region of interest (ROI) of 640 × 720 and a doubled laser double-pulse rate of $f_{\mathrm{Laser}} = 2.5$ kHz at similar particle image density.

Mean and higher order statistics of the near wake of the cylinder are provided in figure 11. A drop-off in the validation rate (figure 11(b)) in the shear layers is due to the loss of correlation in high shear regions. Clearly visible in figure 11(b) are artifacts stemming from the intensity variation of the light sheet which is introduced from below. For EBV a locally reduced intensity is typically associated with a reduction of event rate.

The power-spectrum of the cylinder wake is shown in figure 12 and represents the mean spectrum of all of the domain’s data points using three sequences of 5 s duration. Prominent vortex shedding frequency is present at $f_{\mathrm{cyl}} = 145 \pm 3$ Hz with a Strouhal number $\mathrm{St} = f_{\mathrm{cyl}} d / U_b \approx 0.204$ in good agreement with correlations reported in literature. The spectrum of the vorticity exhibits a second peak at half the shedding frequency ($f_{\mathrm{cyl}}/2 = 72.5$ Hz), which is only weakly visible in the spanwise component v but absent in the streamwise component.

Further insight into the nature of the flow is given through spectral proper orthogonal decomposition (SPOD) which provides a decomposition of the flow both spatially and spectrally [25]. SPOD was performed on the time-records of the two velocity components and out-of-plane vorticity using the *spod_python* package [26]. The spectrum of the first SPOD mode in figure 13 recovers the dominant signals previously observed in figure 12 along with the reconstruction of the corresponding spatial modes (figure 14). At the fundamental frequency f_{cyl} the spatial mode is typical of vortex shedding, whereas the shear layers immediately

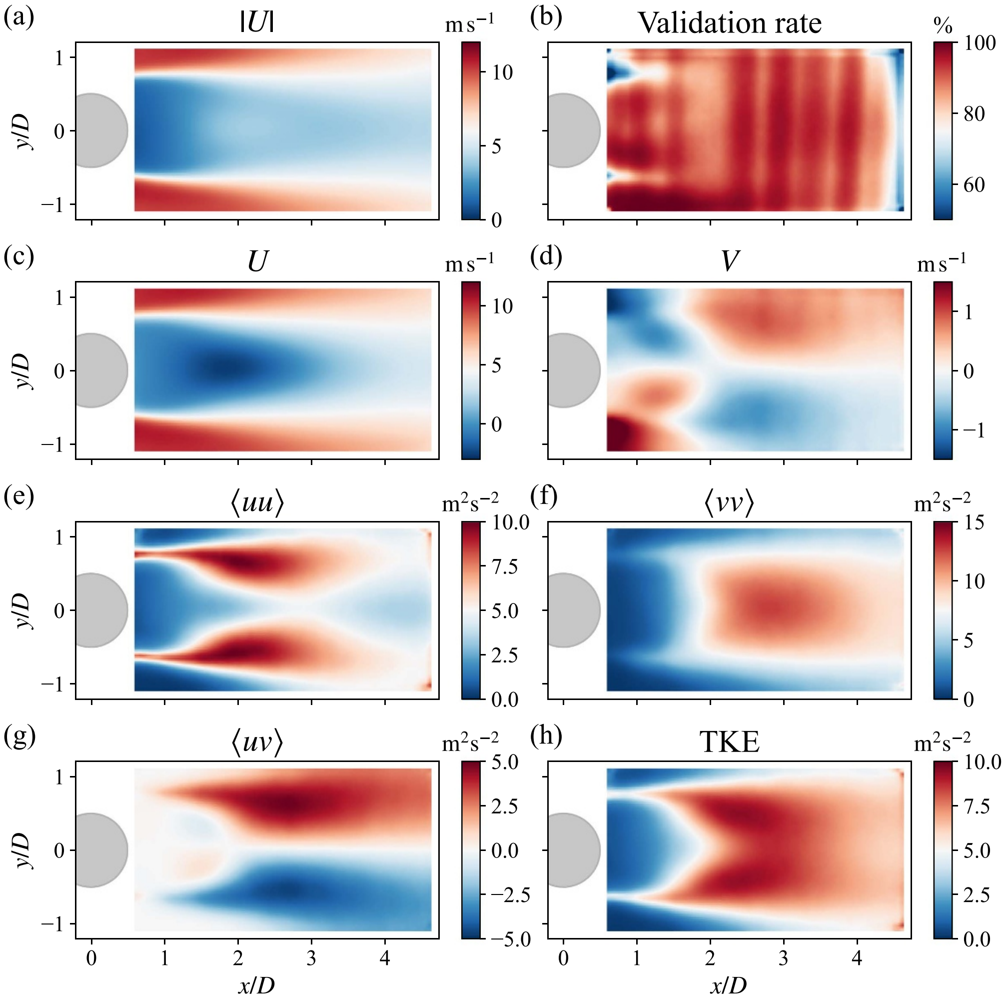

Figure 11. Cylinder wake statistics computed from four 5 s records of $N_{\text{tot}} = 24\,600$ samples acquired at $f_{\text{Laser}} = 1.25\,\text{kHz}$ and $\Delta t = 25\,\mu\text{s}$.

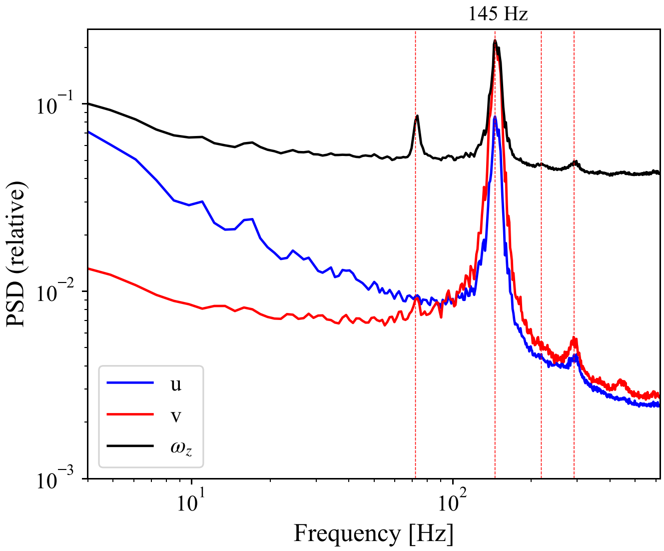

Figure 12. Power spectra of the cylinder wake obtained for both velocity components and the out-of-plane vorticity ω_z.

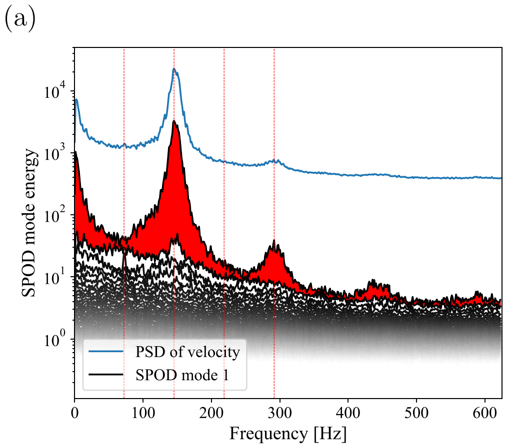

Figure 13. Spectra of the cylinder wake obtained with SPOD, for both velocity components (a) and the out-of-plane vorticity ω_z (b). The mean power spectral density (PSD) as in figure 12.

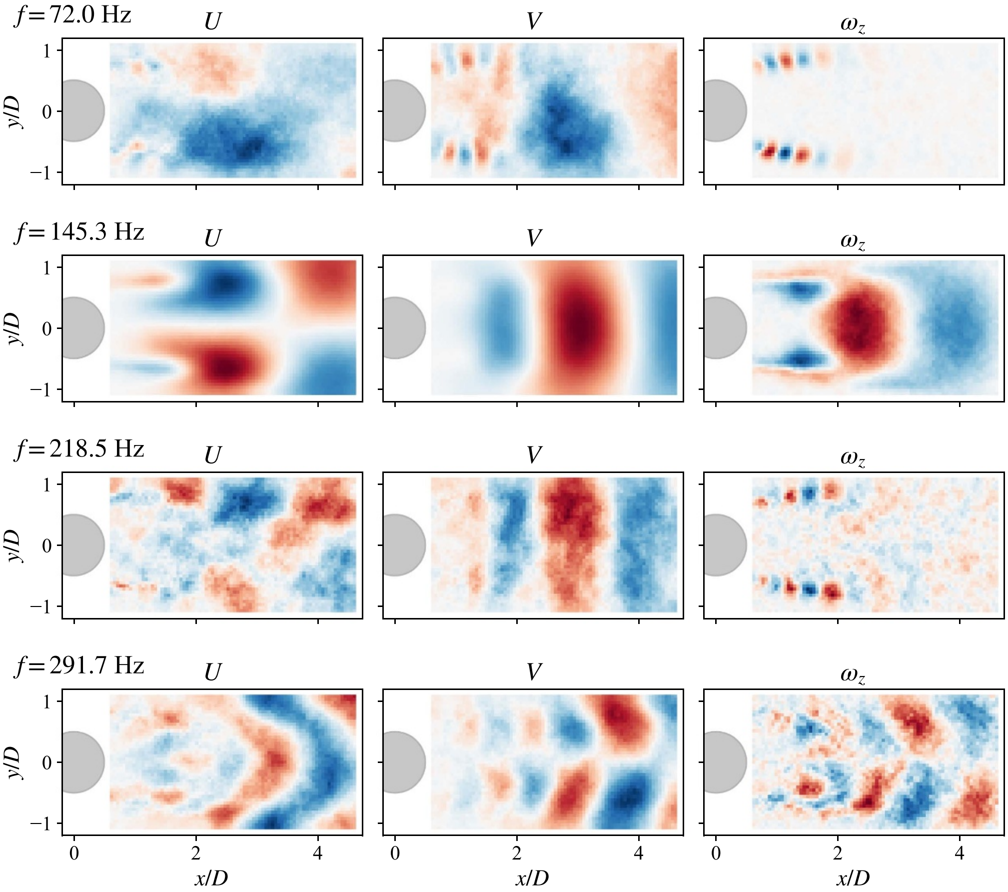

Figure 14. First order SPOD modes of the cylinder wake at representative frequencies indicated in figure 13 for the velocity components U, V and out-of-plane vorticity ω_z.

downstream of the cylinder exhibit distinct flow features at harmonic frequencies $0.5 \cdot f_{\mathrm{cyl}}$ and $1.5 \cdot f_{\mathrm{cyl}}$. At twice the shedding frequency the symmetry of the cylinder wake components reverses with spatial features of roughly half the size of the fundamental mode.

4. Results and discussion

In the course of this study it was found that the presently used hardware based on the Sony IMX636 event sensor is characterized by a maximum readout time t_{read} required to read out all light-pulse induced events. With a range of $t_{\mathrm{read}} = 0.4$–0.5 ms the EBV camera can therefore provide continuous pseudo-image sequences at effective framing rates up to about 2.5 kHz which also has been reported in [13]. By reducing the active sensor ROI the pseudo-framing rate can be increased up to about 10 kHz and is ultimately limited by the EBV sensor's specific latency of 100 µs [2]. By using a pair of event-cameras this capability is extended to provide pseudo-image pairs at the same framing rate. More importantly, the introduced dual-camera setup provides image pairs with arbitrarily chosen inter-framing times Δt well into the sub-microsecond regime which extends the applicability of event-based imaging velocimetry (EBIV) to the transonic/supersonic flow regime.

The bandwidth limitations of the cameras is accompanied by a reduction of the particle image density with increased laser pulsing rate. Measurements at $f_{\mathrm{Laser}} = 1$ kHz provide an optimal trade-off between spatial resolution and pulsing frequency at a particle image density of $\approx$0.01 ppp with particle image diameters of about 2 pixel. The reduction of camera sensor's FOV allows for locally higher spatial resolution and higher laser pulsing frequencies [2]. By tuning of the camera's operating parameters (s.c. 'biases') the data stream can be optimized to reject negative contrast change events in favor of positive event by which the particle image density can be further increased (effectively doubled if only positive events are captured).

Velocity field data determined from binary pseudo-image pairs provided by EBV cameras will be associated with an increased amount of noise in comparison to gray-scale imagery of conventional framing cameras. Comparative studies of EBIV and HSPIV performed by [2, 12] determined that EBIV faithfully reproduces a flow's statistics and dominant spectral content and is well suited for reduced-order modeling.

One of the major advantages of the proposed high-speed EBIV implementation is the continuous streaming capability. In the present setup the pair of cameras streamed about $200\,\mathrm{MB\,s^{-1}}$ at $40 \times 10^6\,\mathrm{Ev\,s^{-1}}$. For a pair CMOS cameras streaming 1280×720 images with 8-bit/pixel at a frame rate of 1 kHz would result in a data rate of $1.7\,\mathrm{GB\,s^{-1}}$. With increasing framing rate (= laser pulsing rate) the data rate from the CMOS cameras would increase proportionally whereas it would remain constant for the EBV cameras due to their bandwidth limitation although the number of particles per pseudo-frame is reduced. The continuous event streams can be transformed to pseudo-frames in real-time with little computational overhead, such that, in principle, velocity maps could be provided in real-time using a sufficiently fast PIV processing engine (e.g. [27]).

Implementing the dual-channel imaging approach with conventional frame-based cameras is possible but can be technically challenging. The triggered frame-capture of most off-the-shelf CMOS cameras with global shutter is limited to the synchronization with the internal line-scan rate which introduces a jitter of several microseconds up to O(100 µs), depending on sensor size and frame rate. The more advanced scientific CMOS cameras require a pre-triggering of several 10 ms to initiate frame capture which is due to the capture of an additional reference frame prior to the actual image capture. When operated in global shutter mode (vs rolling shutter), the actual exposure occurs with a similar line-scan related jitter. Nonetheless, synchronized imaging using an externally provided pixel clock is possible with many of today's high-end high-speed cameras. On the other hand, the herein employed EBV cameras are per se designed to be externally synchronized; the pseudo-framing rate is solely defined by the laser pulsing rate. Moreover, the laser pulsing rate can be adjusted dynamically during event data acquisition, for instance, to capture transient phenomena.

Beyond the high-speed flow measurement presented here the proposed camera configuration is suited for multi-pulse particle tracking such as the 4-pulse 'Shake the Box' (STB) approach [19]. The turbulent boundary layer configuration shown in [19] captured frame-pairs with a $\Delta t = 50$ µs with an interval of 250 µs. This corresponds to 4 kHz which is well within the operational constraints of the utilized event camera.

While not shown herein, the channel separation can also be realized using illumination sources of two different wavelengths, for instance, a green laser operating at a wavelength of 532 nm and a blue laser at 450 nm. On the receiving side the P-BS is replaced with a dichroic mirror which directs the scattered light toward the respective EBV sensors. This approach should be chosen when the tracer particles are not polarization preserving, which is the case for non-spherical particles or large particles outside the Mie scattering regime. Color-based channel separation may also be necessary in situations where the orthogonal polarized nature of the two laser pulses cannot be realized in complex measurement configurations.

5. Summarizing remarks

The measurement approach introduced in the preceding sections addresses the latency limitation of EBV and extends event-based imaging velocimetry (EBIV) to high-speed flows by using two cameras with channel separation, either by polarization of light or by light of differing wavelength. The herein utilized EBV hardware, based on Sony's IMX636 sensor, enables measurement of high-speed flows at up to 10 kHz (at reduced ROI or fewer particle images per pseudo-frame) with essentially no restrictions on the double-pulse separation Δt. Flow field measurements with laser pulse delays down to $\Delta t = 100$ µs and below can be realized. This value is considerably lower than for currently available high-speed cameras which feature inter-framing times of $t_{\mathrm{min}} \geqslant 250$ µs (e.g. Vision Research: T4040 $t_{\mathrm{min}} = 360$ ns, T7510 $t_{\mathrm{min}} = 230$ ns, V2640 $t_{\mathrm{min}} = 490$ ns; Photron: Fastcam Nova S20 $t_{\mathrm{min}} \approx 1000$ ns, Fastcam SA5 $t_{\mathrm{min}} \approx 300$ ns).

The combination of high sensitivity and high-temporal resolution of up to 10 kHz reduces the demands on the illumination side by requiring less laser pulsing energy. Beyond this, the compact packaging and reduced power consumption of O($<$ 1 W) of EBV cameras allows high-speed velocimetry applications in confined environments that previously were inaccessible for bulky high-speed cameras. Compared to currently available time-resolved, high frame rate PIV systems, the hardware cost of the proposed setup is considerably reduced; not only are the cameras roughly an order of magnitude cheaper, their high sensitivity further reduces the investment cost for required light sources. The recent availability of board level event-camera modules allows the assembly of compact dual-sensor cameras. These favorable aspects should enable a more wide-spread use of high-speed velocimetry in both academic and applied research.

Data availability statement

The data that support the findings of this study are available upon reasonable request from the authors.

Altogether the study is based on about 50GB of raw data from various experiments.

Conflict of interest

The author has no financial or personal interests regarding the results of this work.

Funding

The study was entirely supported by DLR internal funding.

ORCID iD

Christian Willert https://orcid.org/0000-0002-1668-0181

References

[1] Willert C and Klinner J 2022 Event-based imaging velocimetry: an assessment of event-based cameras for the measurement of fluid flows *Exp. Fluids* **63** 101

[2] Willert C 2023 Event-based imaging velocimetry using pulsed illumination *Exp. Fluids* **64** 98

[3] Mahowald M 1992 VLSI analogs of neuronal visual processing: a synthesis of form and function *PhD Dissertation* California Institute of Technology, Pasadena (CA) (available at: https://resolver.caltech.edu/CaltechCSTR:1992.cs-tr-92-15)

[4] Mead C 2023 Neuromorphic engineering: in memory of Misha Mahowald *Neural Comput.* **35** 343–83

[5] Gallego G *et al* 2022 Event-based vision: a survey *IEEE Trans. Pattern Anal. Mach. Intell.* **44** 154–80

[6] Chakravarthi B, Verma A A, Daniilidis K, Fermuller C and Yang Y 2024 Recent event camera innovations: a survey (arXiv:2408.13627)

[7] Borer D, Delbruck T and Rösgen T 2017 Three-dimensional particle tracking velocimetry using dynamic vision sensors *Exp. Fluids* **58** 165

[8] Drazen D, Lichtsteiner P, Haefliger P, Delbruck T and Jensen A 2011 Toward real-time particle tracking using an event-based dynamic vision sensor *Exp. Fluids* **51** 1465–9

[9] Howell J, Hammarton T C, Altmann Y and Jimenez M 2020 High-speed particle detection and tracking in microfluidic devices using event-based sensing *Lab Chip* **20** 3024–35

[10] Rusch A and Rösgen T 2023 TrackAER: real-time event-based quantitative flow visualization *Exp. Fluids* **64** 136

[11] AlSattam O A, Mongin M P, Killian A, Gunasekaran S and Hirakawa K 2024 Toward event-based noise-robust high density particle velocimetry *AIAA SCITECH 2024 Forum*

[12] Franceschelli L, Willert C E, Raiola M and Discetti S 2025 An assessment of event-based imaging velocimetry for efficient estimation of low-dimensional coordinates in turbulent flows *Exp. Therm. Fluid Sci.* **164** 111425

[13] Cao J *et al* 2025 Benchmark evaluation of event-based imaging velocimetry using digital micro-mirror device *Exp. Fluids* **66** 73

[14] Sony 2024 IMX636-AAMR datasheet (available at: www.sony-semicon.com/files/62/flyer_industry/IMX636-AAMR-Flyer.pdf)

[15] Finateu T *et al* 2020 5.10 - A 1280×720 back-illuminated stacked temporal contrast event-based vision sensor with 4.86 µm pixels, 1.066GEPS readout, programmable event-rate controller and compressive data-formatting pipeline *2020 IEEE Int. Solid- State Circuits Conf. -(ISSCC)* pp 112–4

[16] Raffel M, Willert C, Kähler C, Scarano F, Wereley S and Kompenhans J 2018 *Particle Image Velocimetry: A Practical Guide* 3rd edn (Springer)

[17] Landreth C C and Adrian R J 1988 Electrooptical image shifting for particle image velocimetry *Appl. Opt.* **27** 4216–20

[18] Kähler C and Kompenhans J 2000 Fundamentals of multiple plane stereo particle image velocimetry *Exp. Fluids* **29** S070–7

[19] Novara M, Schanz D, Geisler R, Voss C and Schröder A 2019 Multi-exposed recordings for 3D Lagrangian particle tracking with multi-pulse Shake-The-Box *Exp. Fluids* **60** 44

[20] Manovski P, Novara M, Mohan N K D, Geisler R, Schanz D, Agocs J, Godbersen P and Schröder A 2021 3D Lagrangian particle tracking of a subsonic jet using multi-pulse Shake-The-Box *Exp. Thermal Fluid Sci.* **123** 110346

[21] Versluis M 2013 High-speed imaging in fluids *Exp. Fluids* **54** 1458

[22] Willert C, Stasicki B, Raffel M and Kompenhans J 1995 Digital video camera for application of particle image velocimetry in high-speed flows *Proc. SPIE* **2546** 124–34

[23] Jakobsen M L, Dewhirst T P and Greated C A 1997 Particle image velocimetry for predictions of acceleration fields and force within fluid flows *Meas. Sci. Technol.* **8** 1502

[24] Murphy M and Adrian R 2010 PIV space-time resolution of flow behind blast waves *Exp. Fluids* **49** 193–202

[25] Schmidt O T and Colonius T 2020 Guide to spectral proper orthogonal decomposition *AIAA J.* **58** 1023–33

[26] Burrows T J 2020 Python SPOD code (available at: https://github.com/tjburrows/spod_python)

[27] Bollt S A, Foxman S H and Gharib M 2025 RapidPIV: full flow-field khz PIV for real-time display and control (arXiv:2504.17987)